



City Research Online

City, University of London Institutional Repository

Citation: Brunhart, M., Soteriou, C., Daveau, C., Gavaises, M., Koukouvinis, P. & Winterbourn, M. (2019). Cavitation erosion risk indicators for a thin gap within a diesel fuel pump. *Wear*, 442-443, 203024. doi: 10.1016/j.wear.2019.203024

This is the accepted version of the paper.

This version of the publication may differ from the final published version.

Permanent repository link: <https://openaccess.city.ac.uk/id/eprint/22724/>

Link to published version: <https://doi.org/10.1016/j.wear.2019.203024>

Copyright: City Research Online aims to make research outputs of City, University of London available to a wider audience. Copyright and Moral Rights remain with the author(s) and/or copyright holders. URLs from City Research Online may be freely distributed and linked to.

Reuse: Copies of full items can be used for personal research or study, educational, or not-for-profit purposes without prior permission or charge. Provided that the authors, title and full bibliographic details are credited, a hyperlink and/or URL is given for the original metadata page and the content is not changed in any way.

City Research Online:

<http://openaccess.city.ac.uk/>

publications@city.ac.uk

Cavitation erosion risk indicators for a thin gap within a diesel fuel pump

Maxwell Brunhart¹, Celia Soteriou¹, Christian Daveau¹, Manolis Gavaises², Phoevos Koukouvinis² & Mark Winterbourn¹

¹*Delphi Technologies, Gillingham, UK*; ²*City, University of London, London, UK*

Abstract

Real industrial examples have been used to evaluate the viability of several cavitation erosion risk indicators (ERIs). Industry standard endurance tests resulted in non-critical cavitation erosion of a shoe and shoe-guide assembly in a high-pressure fuel pump. A design modification was made which eliminated the erosion. Transient CFD simulations of the two designs were run. The distribution and intensity of the resulting ERIs were evaluated against photographic evidence of erosion taken after endurance testing. Details of the component dynamics and the resulting cavitation formation and collapse are presented, along with an analysis of the ERIs for their potential usefulness. Of the 11 ERIs studied, two were found to be particularly good indicators, one of which is newly derived for this research. It is now anticipated that using these ERIs to guide product design and development will save considerable time and cost.

Keywords: cavitation erosion, computation fluid dynamics, erosion prediction, thin gap

1 - Introduction

Cavitation is common in many fields like naval, automotive and aviation, and often leads to problems such as reduced efficiency, noise and erosion. Consequently, there has been extensive research dedicated to understanding and controlling the effects of cavitation, through experiments and CFD simulations. Nevertheless, erosion caused by cavitation is still an ongoing field of research due to the complexity of the physics in the micro and macro scales of cavitation collapse and of the interaction with the boundary material. This, along with the further complexity that simply having cavitation collapse near a solid wall will not always result in erosion, are some of the reasons why there is no consistently accurate model to predict cavitation erosion.

There are numerous articles on the dynamics of a solitary bubble close to a single wall, some early and others more recent (see selectively [1], [2] and [3] among many others). However, the dynamics are significantly different when cavitation is considered in a narrow, liquid filled gap between two walls, which exist for example, in bearings [4], engine cylinders [5] and biological joints [6].

Erosion caused by cavitation has been observed on the boundaries of such gaps, in hardware like gear pumps [7], bearings [8] and engine cylinder liners [9]. However, there is an absence of literature applying cavitation erosion risk indicators (ERIs) to these cases. As such, this paper is dedicated to determining ERIs within a thin, liquid filled gap. A total of 11 potential ERIs were selected for analysis, some from previously published research of other authors and some newly derived for this work. They were assessed on two designs of the same component, one eroding and one non-eroding. Having both of these designs meant a more robust and clear assessment of the potential ERIs was formed, as the CFD results were compared to a non-eroding control case, which is not usually available. Furthermore, the findings were validated against industry examples and so the results have a direct real-world impact.

Considering the works of other researchers investigating cavitation in a thin gap, Gonzalez-Avila et al [10], studied this topic without considering potential erosion. They looked at bubble dynamics between two close parallel surfaces by experimental means. The study used laser induced cavitation and examined the dynamics when a bubble was in contact with one or both sides. They observed that bubbles contacting both walls adopted a cylindrical shape during collapse. These bubbles were produced in a gap of about 50 μ m. The authors also showed that the bubbles contacting both sides collapsed more slowly than bubbles that were only in

Nomenclature

α	Volume fraction (-)	$\bar{\tau}$	Stress tensor (N/m ²)
α_{nuc}	Nucleation site volume fraction (-)	t	Time (s)
c	Speed of sound (m/s)	\mathbf{U}	Velocity vector field (m/s)
F_c, F_e	Empirical constant (m ⁻¹)	V_{cell}	Volume of cell (m ³)
P_a	Acoustic power (W)	ERI	Erosion Risk Indicator (-)
P_p	Potential power (W)	MTR	Mass Transfer Rate (kg/m ³ /s)
p	Pressure (static pressure) (bar/s)	PPD1	1 st definition of potential power density (W/m ³)
p_d	Dynamic pressure (bar/s)	PPD2	2 nd definition of potential power density (W/m ³)
ρ	Density (kg/m ³)	Re	Reynolds number
R_c	Rate of condensing mass transfer (kg/m ³ /s)	Subscripts	
R_e	Rate of evaporating mass transfer (kg/m ³ /s)	l	Liquid
\mathfrak{R}_B	Bubble radius (m)	v	Vapor

contact with one side. Moreover, they point out the importance of viscosity, which is likely to play an important role in collapse time, and thus the energy of collapse. This is not surprising since the importance of viscosity can easily be demonstrated if the Reynolds number (Re) is considered with the characteristic length approaching zero, which would indicate a viscous-dominated flow. This would allow more cavitation to form initially but would also likely slow the collapse.

The effects of viscosity during cavitation collapse were also studied by Quinto-Su et al [11]. They similarly studied laser-induced bubbles in thin gaps experimentally. The authors' work was concerned with biological uses and so used gap widths of 15 to 400 μ m. They found that for bubbles created with the same amount of energy, a smaller gap width resulted in an increase in the lifetime of the bubble.

Hsiao et al [12] used CFD to simulate the collapse of a bubble in contact with two parallel plates. This enabled the gap, of 25 μ m, to be more thoroughly visualized than in experimental studies. Their simulations show that the center region of the bubble collapses faster than the regions near the walls. This results in an hourglass shape near the end of the bubble collapse. Eventually, the vapor region splits into two hemispherical shaped bubbles, one on each wall. This would indicate that cavitation induced erosion is possible on both walls. Moreover, it is accepted that in the general spherical bubble case, the surface tension is insignificant [13]. Hsiao et al went on to state that the effects of surface tension are even less in the bounded bubble than the spherical bubble.

An early work by Parkins & Stanley [14] studied cavitation in an oil film between two oscillating surfaces. They found a characteristic "fern" pattern of vapor was produced. This pattern was also shown by Dellis & Arcoumanis [5] in early stages of cavitation development in the lubrication film between a piston ring and cylinder liner. They went on to show that at higher engine speeds the film thickness would vary, and so different patterns would be formed.

Related to the damage which can be caused by cavitation collapse, Lord Rayleigh [15] indicated that large pressure values occur during vapor collapse. Indeed, researchers have shown that the pressure can exceed 10,000 bar [16] [17]. In more recent years, many researchers have analysed CFD results and calculated parameters to correlate with the erosion. As detailed below, some of those studies focussed on direct forces, like peak pressure attained during collapse, whilst others investigated indirect indicators, like the rate of change of pressure or potential power. Although some success has been shown, there is no confirmation of an overall effective approach. Moreover, attempting to predict the removal of material from the solid boundaries of real components is a significantly greater challenge still. Recent numerical research on potential material damage focusses on the collapse of a single bubble on a simple flat surface [18] [19]. These works calculate either the plastic strain or the plastic deformation and do not extend into material removal. Predicting the removal of material from actual components, particularly those of hardened steel, will heavily

depend on manufacturing processes, geometry and assembly of the component, the effects of which are not currently accounted for in published research.

Regarding parameters to correlate with erosion, Gavaises et al [20] conducted one of the first cavitation erosion studies in fuel injection components and used a bespoke Eulerian-Lagrangian CFD model. They tested two different injector designs that experienced severe erosion in different locations. They were able to show some correlation with the acoustic pressure and liquid volume fraction.

In early experiments by Soda & Tanaka [21], the rate of pressure change appeared to be a likely deterministic factor for cavitation erosion. This idea was investigated numerically by Koukouvinis et al [22] [23] who considered the material derivative of pressure and of liquid volume fraction to investigate erosion in diesel injectors using a commercial Eulerian code. They showed some success in predicting regions at risk of cavitation erosion. Nevertheless, there were some discrepancies with the experimental data which they attributed to the cavitation model. Furthermore, there were no non-eroding designs to compare with to confirm the results. In other works by Koukouvinis et al [24] [25], to improve the cavitation model and limit the negative pressure predicted, they increased the mass transfer rate (MTR). They showed that the maximum values of pressure could be a useful ERI, but again there were no designs without erosion to compare.

Other methods attempting to predict erosion risk examine the energy of the vapor collapse. Franc and Michel [13] and Fortes-Patella et al [26] each considered different energy aspects of bubble collapse and how energy is imparted to a nearby solid surface. However, these two methods appear only to have been applied to a limited degree to flows related to industrial designs, none of which represented a flow in a narrow fluid filled gap.

Considering the definitions of some erosion indicators, which are discussed in section 4.1, it may be expected that there will be some dependence on the resolution of the numerical grid used in CFD simulations. Indeed, Mihatsch et al [27] explored the effects of mesh refinement on a possible cavitation erosion indicator related to maximum pressure. They ran a parametric study with simulations of three different mesh refinements on a well-studied test geometry. The researchers showed that continued mesh refinement resulted in resolving smaller scale vapor structures, though this did not have a major impact on their ERI results. While agreement with experiments was achieved, the CFD results were calibrated using a scaling factor. Furthermore, there was not a non-eroding design to benchmark their results.

The work detailed in this paper involves a component within a high-pressure fuel pump [28]. It was noted by the Delphi Technologies Pump Team, following endurance tests, that some slight cavitation erosion occurred on the shoe and shoe-guide, which are located under the pumping plunger. The current work investigates erosion of the boundaries of this narrow fluid filled gap and the application of potential ERIs.

The details of this assembly and the endurance test findings are given section 2, while section 3 explains the dynamics of the shoe within its guide during normal operation. Although the erosion after endurance testing was too slight to result in a problem over the life of the pump, alternative designs were investigated in the interest of robustness for future applications with increased requirements. Some of the designs were successful in avoiding cavitation erosion and showed no signs of damage after testing.

To understand this erosion, a CFD investigation was undertaken on the fluid filled gap between the shoe and guide. Section 4 describes how both the original design and an alternative design, which avoided erosion, were modeled. Section 4.1 defines the parameters examined, referred to here as ERIs, which were used to assess the potential risk of surface erosion. The CFD simulations examined the cavitation characteristics within the dynamic gap between the shoe and guide faces and the results are discussed in section 5. Section 5.1 describes how each ERI was evaluated by comparing the distribution of its maxima to images of the damaged components. Finally, the summary and conclusion are given in section 6.

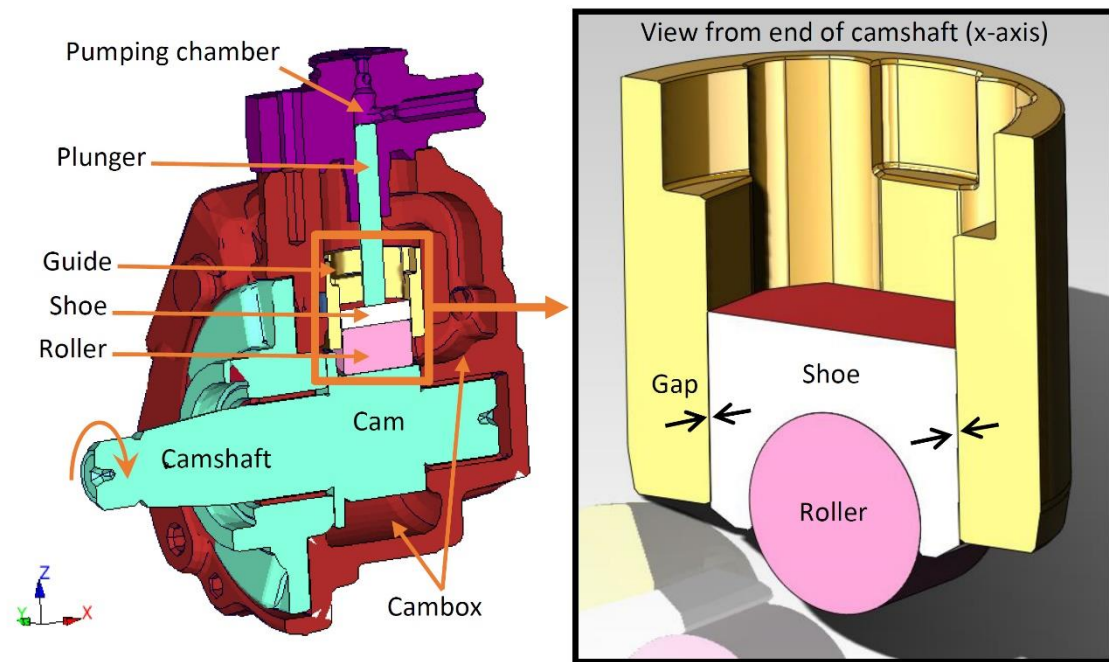


Fig. 1 - Cutaway diagram of the fuel pump and the location of the shoe and shoe-guide within.

2 - Experimental procedure and results

Fig. 1 shows a cutaway of the high-pressure fuel pump and the location of the narrow gap between the sliding faces of the shoe and the guide. The pump pressurizes fuel up to 2000 bar and delivers it to the common rail system [29]. Newly designed or modified components undergo extensive testing before they can proceed to serial production. Endurance runs form part of this testing, which assess the robustness of the component when exposed to long periods of continuous running at demanding operational conditions. One such endurance test runs the fuel pump at 5000 RPM for a time period that is orders of magnitude longer than the

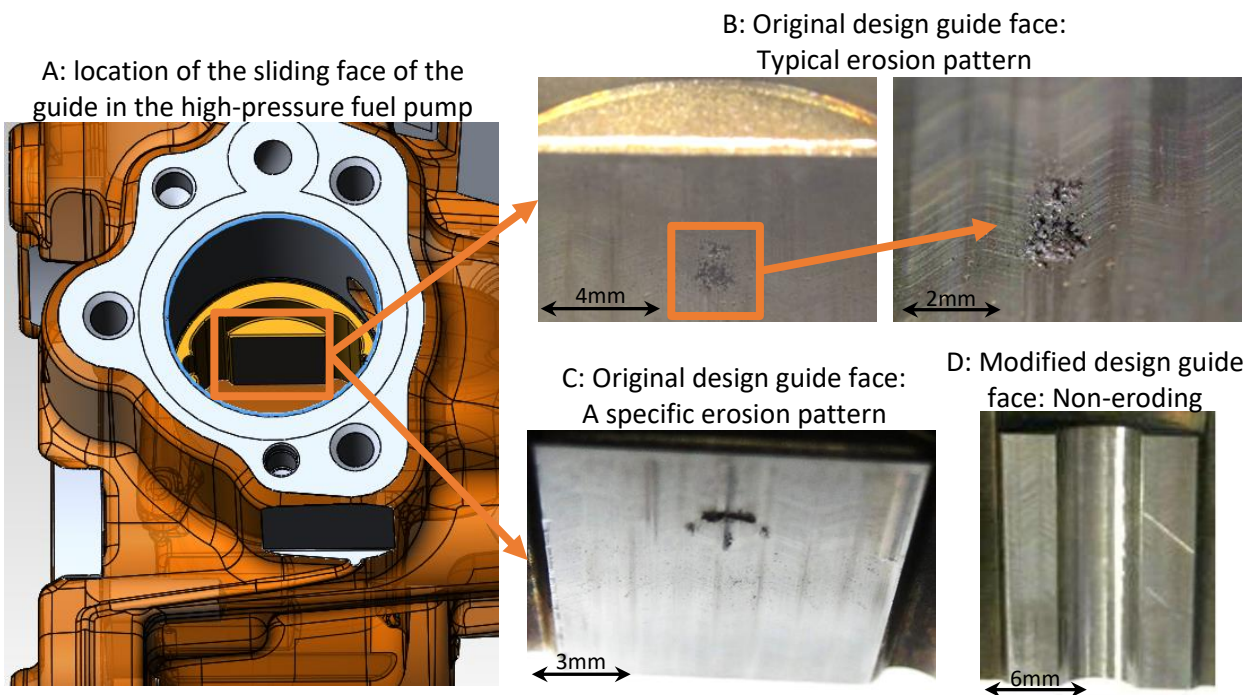


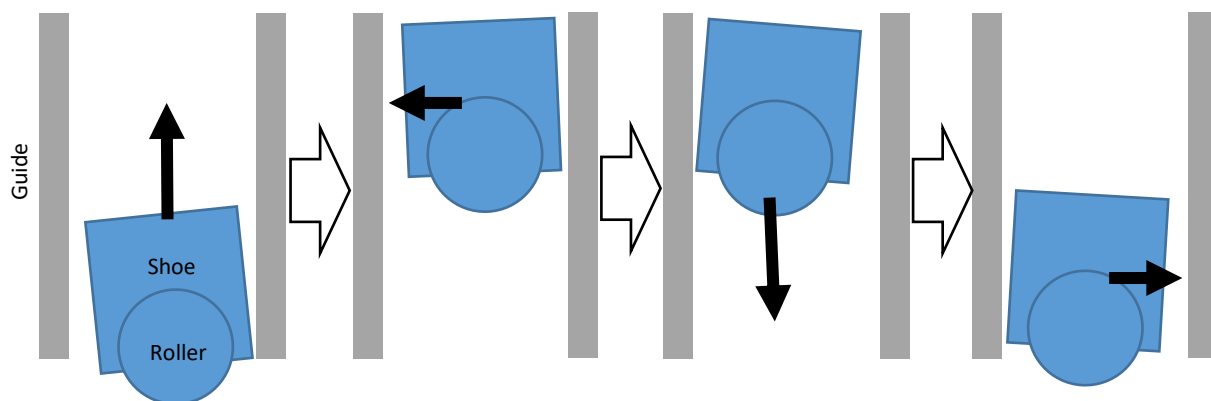
Fig. 2 – Examples of the non-critical cavitation erosion, or lack thereof, on the two designs

time spent at any running condition in normal use. After this test it was found that the guide face experienced varying patterns of non-critical cavitation erosion. Fig. 2-B shows the typical pattern of damage found on the face of the guide, while Fig. 2-C shows a specific pattern seen on one sample. Fig 2-C also shows clearly the simple, flat-face geometry of the original design. Although the erosion was too slight to result in a problem over the life of the pump, alternative designs were investigated in the interest of robustness for future applications with possibly increased requirements. One such proposed design had a large vertical groove on the face of the guide (Fig. 2-D). Subsequent endurance tests with this modified design resulted in the elimination of erosion on the faces of the shoe and its guide. The guide is made of steel with surface hardening by sintering in accordance with ISO 5755 FD-05N2C-950H.

3 - Geometry and dynamics of the shoe and shoe-guide assembly

Referring to Fig. 1, as the camshaft rotates during the pumping stroke, the cam vertically displaces the roller, shoe and plunger, which pressurises the fuel in the pumping chamber (Fig. 3-A). After the top of the stroke, the cam profile and the return spring allow the plunger assembly to retract to its original position, enabling the pumping chamber to refill for the next stroke (Fig. 3-C). With this type of pump design, there is a small, yet interesting, lateral movement of the shoe within the guide. The lateral movement is caused by the direction of the force transmitted to the shoe from the rotating cam, via the roller. This lateral thrust causes the shoe to travel at a slight angle within the guide, during both the pumping and filling periods. When the plunger reaches the top of its stroke, the direction of the thrust from the cam changes, which causes the shoe to change its tilt angle and move across the small clearance within the guide (Fig. 3-B). The gap between the shoe and its guide is fluid filled and is fed by the cambox on all four sides. When the shoe moves away from its guide due to the lateral force, albeit by only tens of microns, the fluid pressure will be reduced. If the flow from the cambox is then unable to fill the increasing volume in the gap at the appropriate rate, cavitation will be generated. It was expected that this possible cavitation creation and its subsequent collapse is what led to the erosion seen on the hardware after endurance tests.

An elastohydrodynamic (EHD) simulation of some of the high-pressure pump components was previously commissioned by Delphi Technologies [30]. As part of that, the linear and rotational components for the shoe



A – Pumping stroke: the shoe is pushed upward due to the rotation of the cam. This moves the plunger which compresses the fuel. The thrust from the cam causes the shoe to tilt.

B – Top of stroke: the shoe is forced laterally across the guide clearance due to the change in direction of the thrust from the cam. This also changes the shoe tilt.

C – Filling stroke: the cam profile and return spring allow the plunger assembly to retract to its original position, enabling the pumping chamber to refill for the next stroke.

D – Bottom of stroke: the shoe returns to begin the pumping cycle again.

Fig. 3 - Schematic indicating the shoe motion within its guide during a pumping cycle.

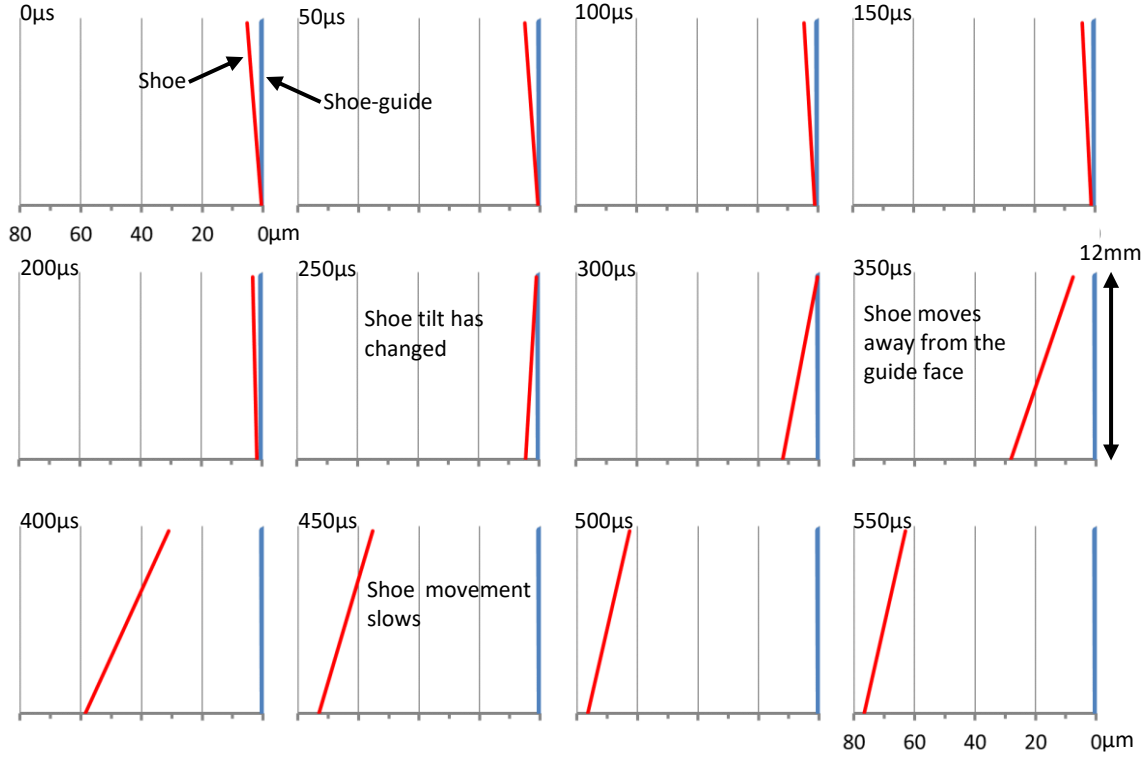


Fig. 4 - 2D visualization of the change in shoe orientation at the top of the pumping stroke.
(Note the x-axis scale is in μm while the y-axis scale is in mm .)

movement were calculated. Although both sides of the shoe are affected by this lateral motion (Fig. 3-B and D), it is the side that is in closest contact during the pumping stroke which is of more interest (Fig. 3-B). Further detailed visualization of the shoe face movement is given in Fig. 4. The shoe movement shown in Fig. 4 occurs close to top of the pumping stroke and corresponds to Fig. 3-B. The gap clearance ranged from $0.4\mu\text{m}$ to $79\mu\text{m}$.

4 - Simulation model and methodology

All simulations were done with ANSYS Fluent V17 (see [31] for details) where the mass and momentum conservation equations (Eq. 1 and Eq. 2, respectively) are given as:

$$\frac{\partial \rho}{\partial t} + \nabla \cdot (\rho \mathbf{U}) = 0 \quad \text{Eq. 1}$$

$$\frac{\partial (\rho \mathbf{U})}{\partial t} + \nabla \cdot (\rho \mathbf{U} \mathbf{U}) = -\nabla p + \nabla \cdot (\bar{\bar{\tau}}) \quad \text{Eq. 2}$$

where \mathbf{U} is the velocity vector field, t is time, p is pressure, ρ is the density and $\bar{\bar{\tau}}$ is the stress tensor.

To model the cavitation effects, an additional transport equation for the vapor phase is solved, defined as:

$$\frac{\partial (\alpha_v \rho_v)}{\partial t} + \nabla \cdot (\alpha_v \rho_v \mathbf{U}_v) = R_e - R_c \quad \text{Eq. 3}$$

where α_v is vapor volume fraction, the subscript v denotes vapor and R_e and R_c denote evaporating and condensing MTR, respectively. The mass transfer terms (R_e and R_c) are defined by the Zwart-Gerber-Belamri (ZGB) model, first described by Zwart et al [32], are given as:

$$R_c = F_c \frac{3\alpha_v \rho_v}{\mathfrak{R}_B} \sqrt{\frac{2(p - p_v)}{3\rho_l}} \quad \text{Eq. 4}$$

$$R_e = F_e \frac{3\alpha_{nuc} \alpha_l \rho_v}{\mathfrak{R}_B} \sqrt{\frac{2(p_v - p)}{3\rho_l}} \quad \text{Eq. 5}$$

where \mathfrak{R}_B the bubble radius, F_c and F_e are empirical constants, α_{nuc} is the nucleation site volume fraction and the subscripts v and l denote vapor and liquid, respectively. When the simulations were run, unrealistic negative pressures did not occur. This indicates it was unnecessary to calibrate the cavitation parameters further [33], therefore the default values of \mathfrak{R}_B , α_{nuc} , F_e and F_c were used [31].

The geometry of interest in the original design was a hexahedron, created by the two flat faces of the shoe and its guide and the narrow, uneven gap between them. The faces were approximately 12mm square and the fluid filled gap was fed by the cambox pressure on all four sides. Considering the narrow gap range of $0.4\mu\text{m}$ to $79\mu\text{m}$ and the flow rates under investigation, the flow regime was expected to be largely laminar, which calculations confirmed. This can affect the structure of cavitation formed [34].

As with the actual components, the guide face remained stationary for the simulation, while the shoe face moved to vary both the gap width and the tilt, with respect to the guide. The modified design had the same shoe face and the same motion profile but had a semi-circular vertical groove in the guide face. A deforming mesh was implemented to accommodate the shoe movement, as described in section 3. The simulations begin near the top of the pumping stroke Fig. 3-B) and run over a period of $880\mu\text{s}$.

Fig. 5 shows the mesh within the groove and the narrow gaps. The detail shown in the enlarged section for the narrow gap was used in both designs. The gap was divided into 20 cells to ensure appropriate resolution. Cell aspect ratio was of course a concern, but care was taken to impose a well-structured deforming mesh as the gap expands and the flowrate increases.

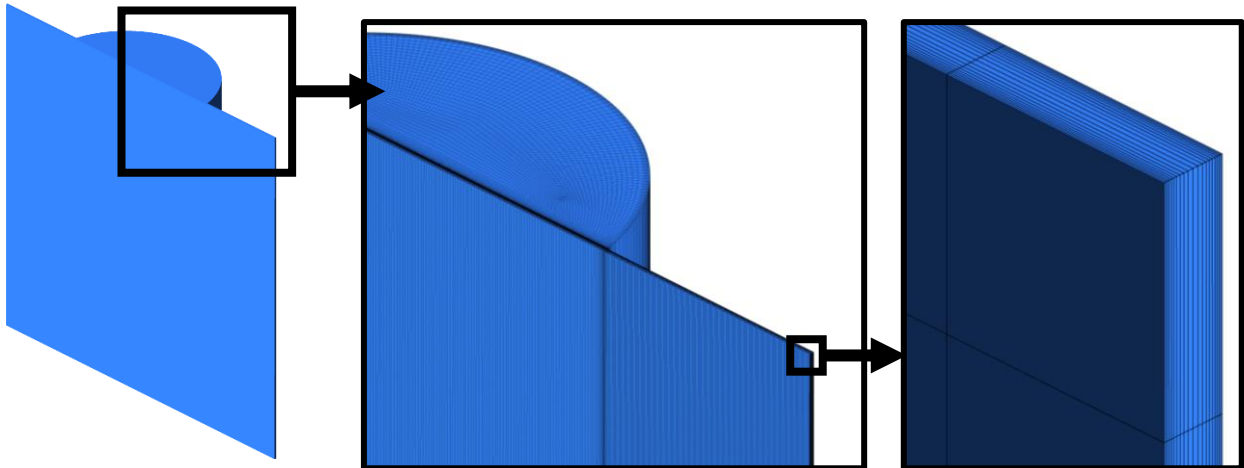


Fig. 5 - Mesh of the groove in the guide face and of the narrow gap between the faces of the shoe and the guide.

A mesh study was carried out on the original design. It was seen that a symmetrical boundary down the centre gave results which were almost identical to those of simulations with the full domain. Different levels of mesh refinement were considered, from 68 thousand to 3.6 million cells. These changes had almost no effect on flowrate and so the coarsest mesh

could be considered to provide a mesh independent result. However, while flowrate may be an adequate variable to determine mesh independence for many simulations, it may not be an acceptable criterion for some of the ERIs being investigated. As such, for the final simulations, the finest mesh was selected. Hence, the original design had approximately 3.6 million cells and the modified design had about 5.2 million cells.

The pressure boundary condition of four bar was applied to the four sides and matched the averaged values measured in the cambox during regular operation. The fluid properties were modelled as Normafluid (ISO4113), the standard test fluid in the diesel industry and what was used in the endurance tests. These were based on [35] and [36] and previously used by Bush et al [37] in experimentally validated CFD simulations. Reference values at 4 bar and 100°C are given in Table 1. Given the high pressures expected during cavitation collapse, liquid compressibility was included.

Table 1 – Fluid properties at 4 bar and 100°C.

Property	Liquid (l)	Vapor (v)
Density (kg/m ³)	764	6
Bulk modulus (bar)	8896	
Speed of sound (m/s)	1079	
Dynamic viscosity (kg/m/s)	8.5e-4	4e-6

4.1 - Erosion risk indicators

Many factors relating to erosion risk have been suggested in the literature. Some relate to forces experienced, while others relate to the potential energy or power of the violently collapsing vapor region. The published indicators reviewed and tested in the current work are from Franc & Michel [13], Fortes-Patella et al [26] and those applied to diesel injectors by Koukouvini et al [25] [22]. This work also explores several other variables and their derivatives.

Pressure (i.e. static pressure) was considered as a possible ERI. The material derivative of this, and of dynamic pressure, density and liquid volume fraction were also evaluated. The material derivative is given as:

$$\frac{D\varphi}{Dt} = \frac{\partial\varphi}{\partial t} + \mathbf{U} \cdot \nabla\varphi \quad \text{Eq. 6}$$

where φ is the variable of choice. Clearly, the material derivative includes terms related to time and the fluid motion. It is important to include the latter term to account for the fact that a region of vapor could be moving from a specific position due to fluid motion, rather than that vapor collapsing. An easily obtainable ERI also considered was the MTR during condensation (R_c in Eq. 4) which is strongly linked with the derivatives of density and liquid volume fraction.

An energy approach was first postulated by Hammitt [38] and expanded on by Fortes-Patella et al [26]. The latter work presented a means of measuring cavitation aggressiveness by considering the potential power density (P_{p1}/V_{cell} or $PPD1$), defined as:

$$\frac{P_{p1}}{V_{cell}} = (p_v - p) \frac{\partial\alpha_l}{\partial t} + \alpha \frac{\partial p}{\partial t} \quad \text{Eq. 7}$$

where V_{cell} is the cell volume. This comes from the derivative of potential energy of a bubble. The authors went on to assume the $\partial p/\partial t$ term was negligible. Moreover, from the local mass equation ($\partial\rho/\partial t + \rho \text{div}(\mathbf{U})$) Eq. 7 can be rearranged to get a second form of potential power density ($PPD2$), defined as:

$$\frac{P_{p2}}{V_{cell}} = (p_v - p) \frac{\rho}{\rho_l - \rho_v} \text{div}(\mathbf{U}) \quad \text{Eq. 8}$$

While Eq. 8 was the final derivation used by Fortes-Patella et al, Eq. 7 was also tested for its potential as an erosion indicator.

An alternate energy approach was considered by Franc & Michel [13]. Their equation quantifies the acoustic power (P_a), defined as:

$$P_a = \frac{\rho_l V_{cell}^2}{4\pi c_l} \left(\frac{\partial^2 \alpha_l}{\partial t^2} \right)^2 \quad \text{Eq. 9}$$

when expressed in terms of cell volume and liquid volume fraction. Here, c_l is the speed of sound in the liquid.

The above potential ERIs were assessed by examining the magnitude and distribution of maximum values reached during the simulation periods and comparing the results to images of erosion. While the magnitude of these indicators may still be affected by the mesh or time-step, the difference in the relative values between the two designs should still be preserved. The overall objective is a high level of differentiation between the two designs in the relative magnitude of the ERIs, with strong correlation of maxima locations with erosion as seen on the hardware.

5 - Results and discussion

The results for the original design are given in Fig. 6. The time evolution of pressure, velocity, liquid volume fraction and condensing MTR are shown. These results are provided on the mid-plane in the gap. The first frame in Fig. 6, at $187\mu\text{s}$, shows the initial effects of the lateral shoe movement. As the shoe changes its angle, pressure is building at the top, as that region is compressed. Near the bottom, cavitation is being produced as the fuel flowing into the ultra-narrow gap cannot keep up with the expanding volume. Although this initial lateral movement has these noticeable effects, it is too small to be discernible in Fig. 4. At $307\mu\text{s}$, the shoe is pulling away from the guide at such a rate that the entire gap has cavitated. By $487\mu\text{s}$, the movement of the shoe slows and the fuel flow from the cambox at the boundaries is collapsing the vapor. On the next frame, $547\mu\text{s}$, all the vapor has collapsed. The pressure caused by the inward force from this initial collapse rebounds outward, resulting in the creation of a second vapor region followed by its collapse. The initial vapor collapse and rebound are shown in detail in Fig. 7, where the distinct shape of the collapsing cavity is clear.

The velocity images on the later frames in Fig. 6 and Fig. 7 show a skewed cross region. This is where the flow from the four sides meet, which gives rise to the four fingers of liquid growing into the vapor region during the collapse (Fig. 7). This characteristic also produced a cross-shape in some of the ERIs, shown later.

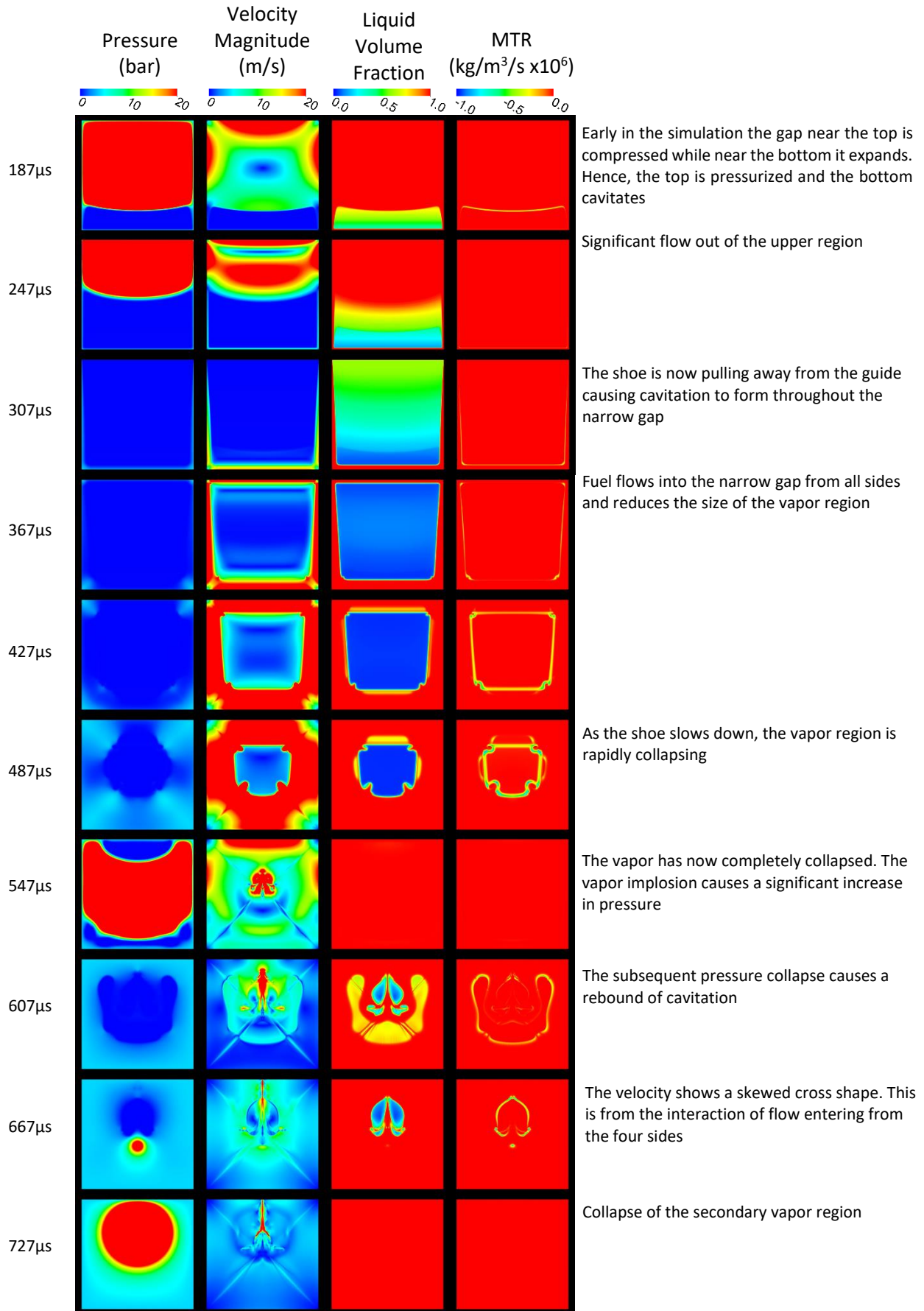


Fig. 6 – Original design: full cycle sequence of cavitation creation, collapse and rebound.

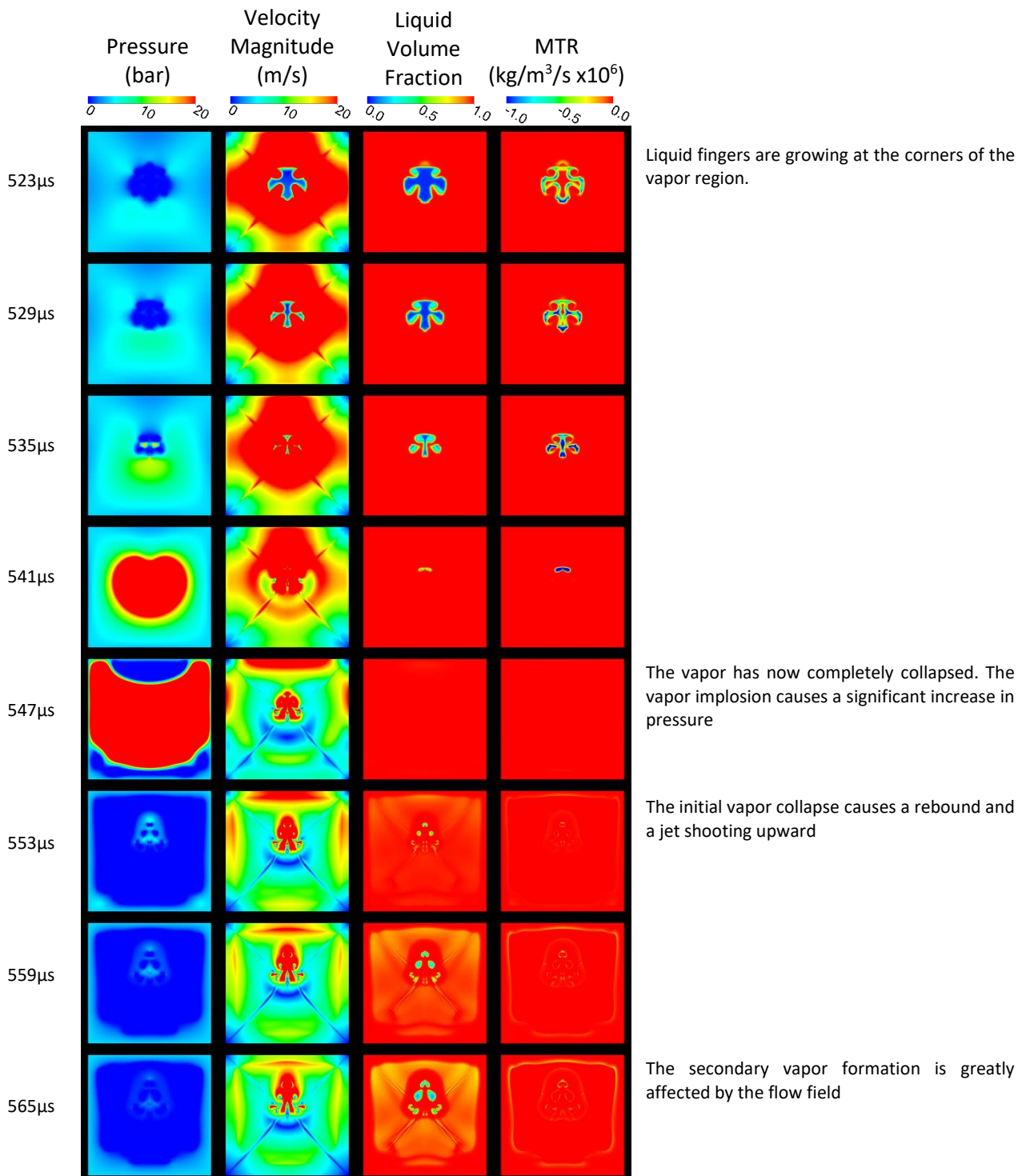


Fig. 7 – Original design: detailed sequence of the initial vapor collapse and rebound.

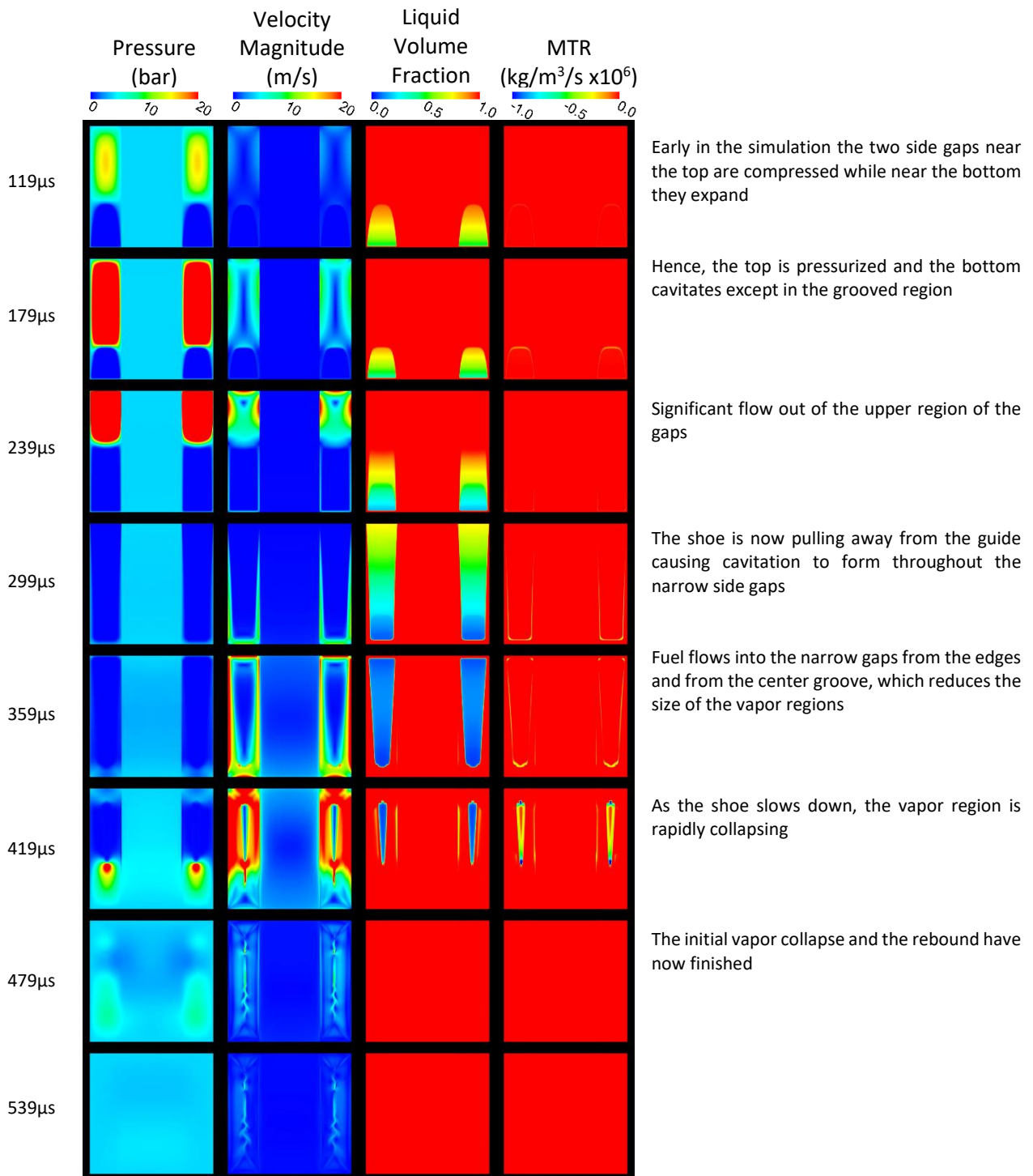


Fig. 8 – Grooved design: full cycle sequence of cavitation creation and collapse.

Fig. 8 shows the cycle of cavitation within the grooved design. By 119 μs the effects of the shoe movement are apparent, with pressure increasing near the top and cavitation being produced near the bottom. With this design though, the cavitation is noticeably isolated to the two thin gaps, with no vapor being created in the grooved region. By 299 μs, as with the original design, the narrow gaps have almost completely cavitared. However, the vapor completely condenses much earlier than in the original design. A detailed view of the vapor collapse in the grooved design (Fig. 9) shows almost all the initial vapor has condensed by 437 μs, about 90 μs before the original design. By 449 μs, a vapor rebound occurs, but is smaller than that produced in the original design.

The difference in collapse time is attributed to the amount and distribution of cavitation formed and the locations where fuel from the cambox can flow into the narrow gap. The groove itself does not cavitate, as the shoe only moves a few microns and so the percentage volume change within the groove is minimal. However, for both designs, the percentage volume change in the gap is significant, and cavitation occurs because the flow from the cambox is insufficient to suppress it.

It can be concluded that in general, the groove in the modified design significantly reduces the region of the narrow gap and increases the access to the cambox pressure. This access reduces the overall amount of cavitation formed in the first place and enables an earlier collapse. However, while these factors are significant, they do not indicate if erosion will occur. Hence the need for validated ERIs.

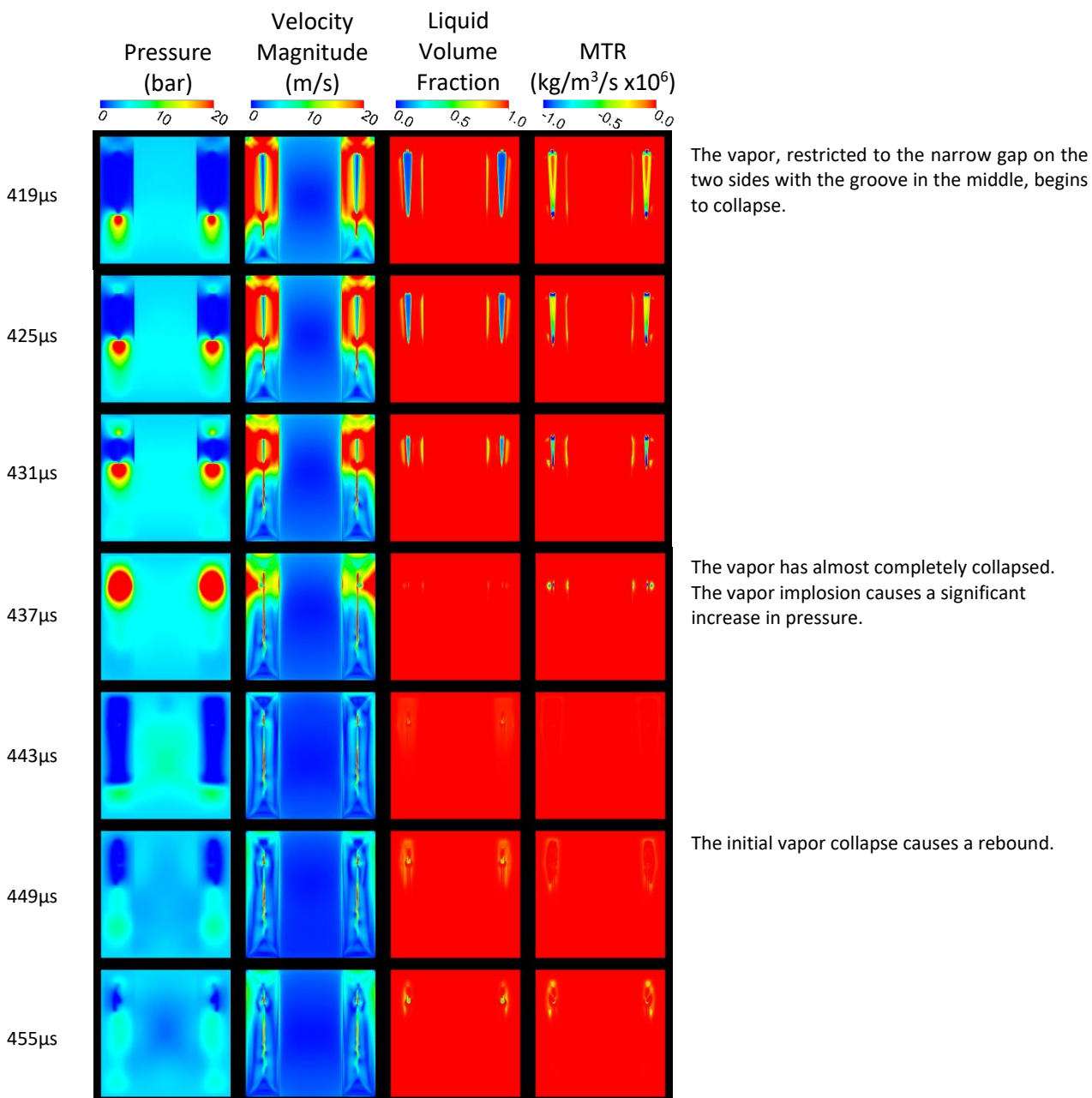


Fig. 9 – Grooved design: detailed sequence of the initial vapor collapse and rebound.

5.1 - Erosion risk indicators

The maximum values related to pressure that occurred throughout the simulation period are presented in Fig. 10. This shows the pressure and its derivatives: p , Dp/Dt , D^2p/Dt^2 and $(Dp/Dt)^2$, for both the original and the grooved design.

The maxima of pressure, p , seen in the first column of Fig. 10, experienced a peak of 1480 bar for the original design and 875 bar for the grooved design. However, these peak values are caused by the shoe movement compressing the fuel early in the simulation (Fig. 11) and are not associated with cavitation collapse. Moreover, these values clearly do not exceed the pressure the material would be expected to withstand.

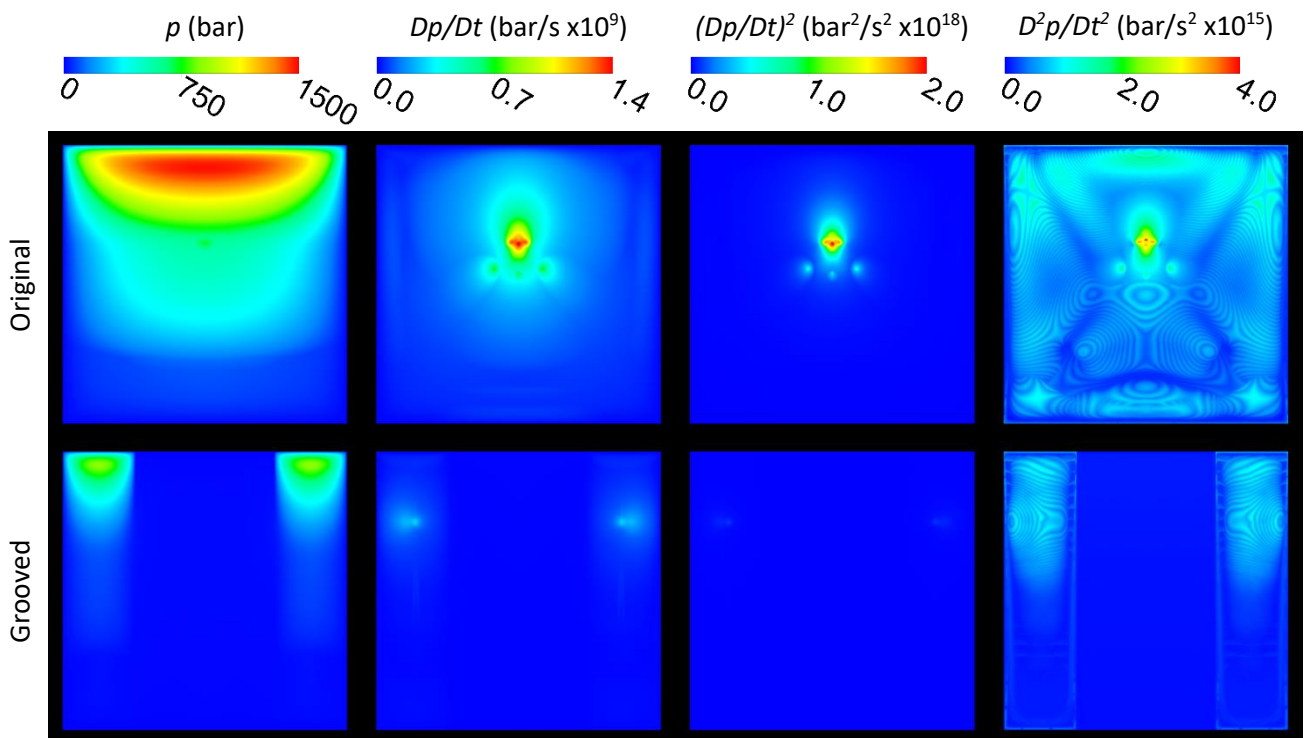


Fig. 10 - Potential ERIs: maximum values reached throughout the time period.

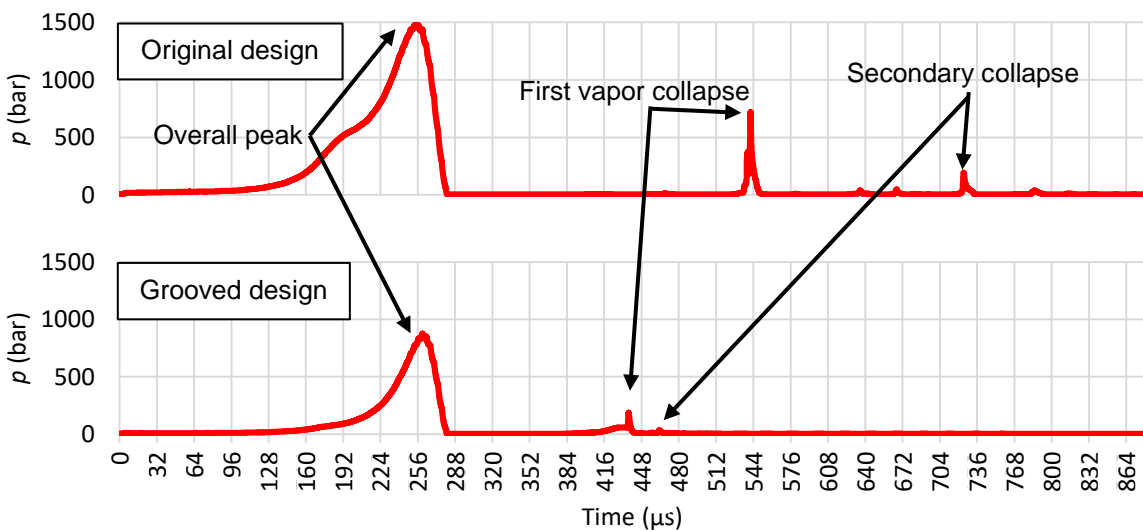


Fig. 11 – Maximum values of pressure on the wall during the simulation period.

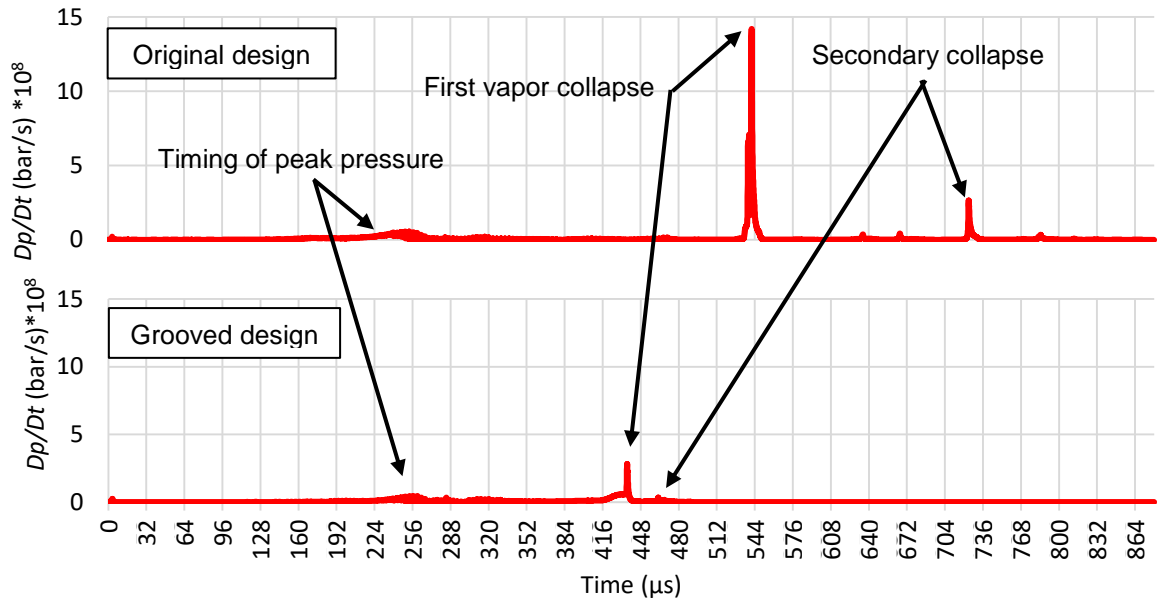


Fig. 12 – Maximum values of Dp/Dt on the wall during the simulation period.

These results differ from those of some other researchers who used pressure as an ERI (for example [25]). However, defining absolute values for which damage will occur, rather than relative values or frequencies of occurrence, has significant uncertainties for different components, assemblies and methods of manufacture. Furthermore, fluid properties are not known for pressures of several thousand bar, which affects the predicted pressure values. As such, absolute maxima of pressure is not a reliable ERI here. However, the spike produced during vapor collapse indicates that the rate of pressure change could be a useful indicator.

The second column in Fig. 10 shows the distribution of maximum Dp/Dt for the two designs. A clear peak is seen on the original design and its location coincides with that of the erosion on the hardware (Fig. 2). Moreover, Fig. 12 shows that this peak occurs during the collapse of vapor. The peak value reached was $14e8$ bar/s. There is also some activity on the grooved design, but at $2.8e8$ bar/s it is significantly lower than in the original case. These results show that Dp/Dt is useful as an ERI. The third column in Fig. 10 shows maxima of $(Dp/Dt)^2$, which further accentuates the differences between the two designs seen with Dp/Dt . This ERI, $(Dp/Dt)^2$, is newly derived for this work and provides distinct advantages.

The fourth column in Fig. 10 shows the maxima of D^2p/Dt^2 . The CFD results show high values that correlate well with where erosion was found on the original design hardware, but there is also a lot of activity elsewhere in the domain. As such, D^2p/Dt^2 does not provide a better indication of erosion risk than Dp/Dt .

The maxima for the derivative of dynamic pressure, Dp_d/Dt is shown in Fig. 13. On the original design, the location of the peak Dp_d/Dt lines up well with the region of erosion. However, similar values are reached with the grooved design. Thusly, for this component at least, the derivative of dynamic pressure is not considered a viable ERI. As expected, the overall peak values reached are substantially less than its static pressure counterparts.

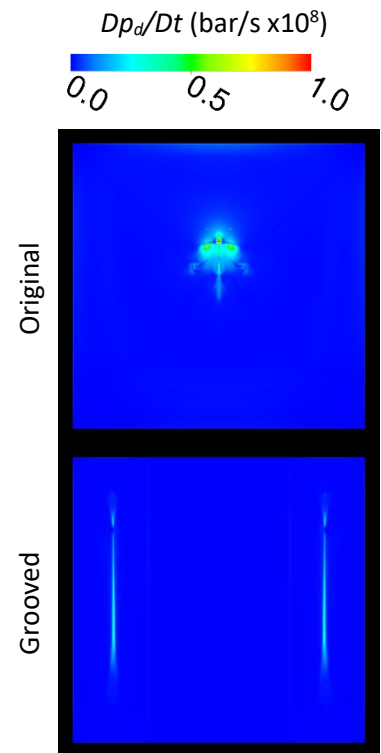


Fig. 13 - Potential ERI: maximum values reached throughout the time period.

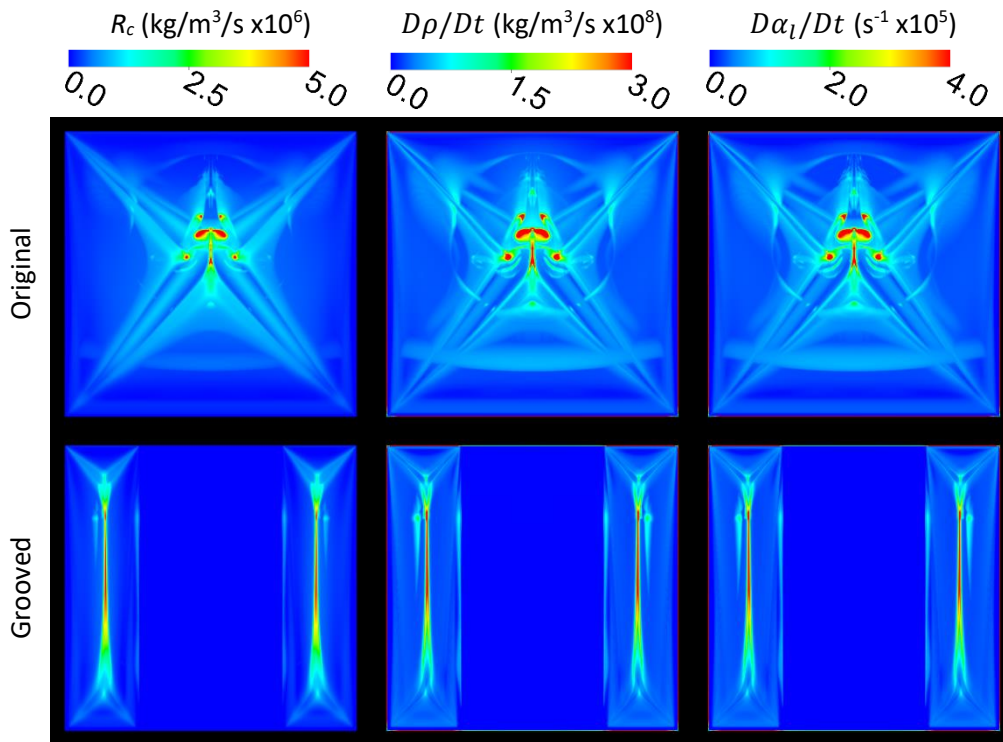


Fig. 14 - Potential ERIs: maximum values reached throughout the time period.

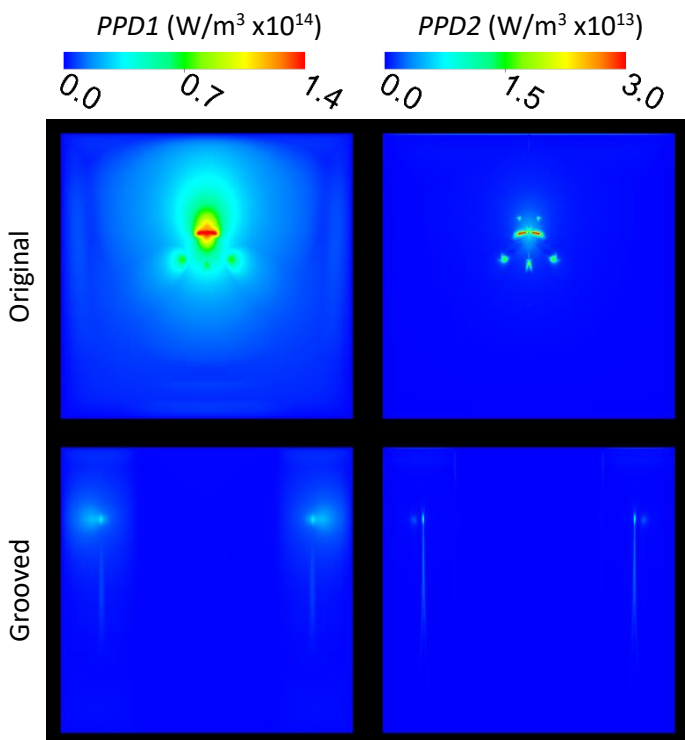


Fig. 15 - Potential ERIs: maximum values reached throughout the time period.

The MTR during condensation (R_c) and the derivatives of density ($D\rho/Dt$) and liquid volume fraction ($D\alpha_l/Dt$) were also considered as potential ERIs (Fig. 14). As mentioned earlier, a skewed cross-shape is notable. This cross was produced as the inward flow from the boundaries impinged on each other. Unsurprisingly, the maximum values of these indicators produced similar contour images. For all three potential ERIs, the original design has maxima in the location of erosion, but the grooved design has similar values where there was no cavitation erosion present on the hardware after endurance tests. Hence, these parameters do not show potential as ERIs for this component.

Derivations from other researchers' published work were also considered for their potential as ERIs. Accordingly, the distribution of maxima of potential power density, $PPD1$ (Eq. 7), and $PPD2$ (Eq. 8) and from acoustic pressure, P_a (Eq. 9) were calculated. The maxima of $PPD1$ are shown in the first column of Fig. 15, and resemble those of Dp/Dt , seen

earlier in Fig. 10. This indicates that the partial derivative of pressure, $\partial p/\partial t$, is the dominating term for this parameter. It does not offer anything more than the material derivative, Dp/Dt .

The distribution of maxima for *PPD2* is shown in the second column of Fig. 15. The result for *PPD2* is somewhat different from that for *PPD1*, even though they are both definitions of potential power density. *PPD2* shows a clear difference between the original and grooved designs. Moreover, on the original design, *PPD2* produces a clear shape that resembles the distinctive erosion pattern seen on a particular hardware sample, shown in Fig. 2 - C. Hence, *PPD2* is a good ERI and provides clearer results than *PPD1*.

Although the plots in Fig. 11 and Fig. 12 show results on the surfaces of the shoe and guide, all the CFD images shown so far have been on the mid-plane between the shoe and the guide. The ERIs directly on the faces of the shoe and the guide were also investigated but did not change the assessments for 10 out of the 11 ERIs. P_a was the one exception, as seen in Fig. 16. The distribution of the maxima on the mid-plane could indicate that P_a would be a reliable ERI, with high values only in the region of erosion on the original design. However, unlike the other ERIs considered, the results on the shoe surface contradict this. The maxima on the shoe surface on the grooved design reach similar values as the original design, which indicates that P_a would be misleading as an ERI.

The qualitative assessments of the different ERIs tested are summarized in Table 2. ERIs that did not provide a clear difference between the prototype and modified design are labelled “poor.” ERIs that provided the clearest difference between the two designs, and where the locations of the maxima correlated well with erosion seen on the hardware, are labelled “good.” The other erosion indicators are labeled “some” as they provide only a limited indication of erosion potential.

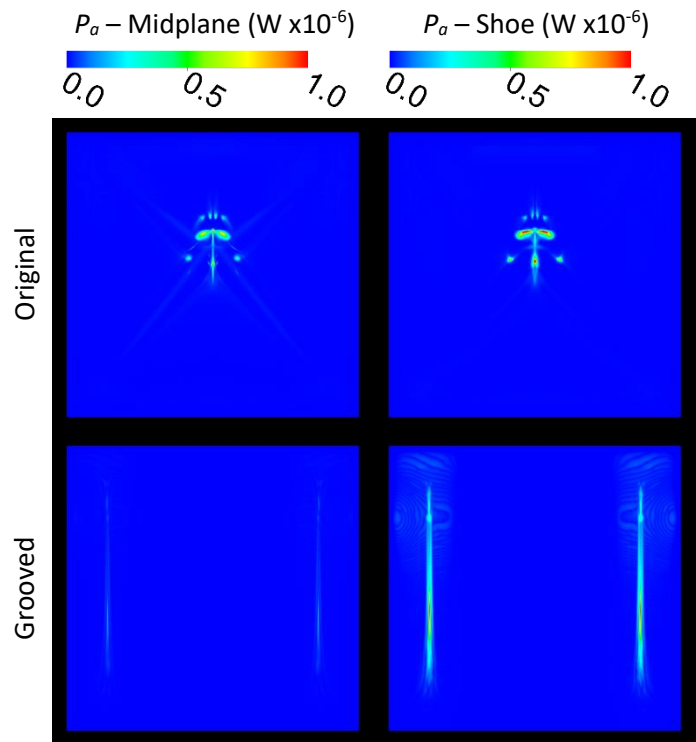


Fig. 16 - Potential ERI: maximum values reached throughout the time period.

Table 2 – List of potential ERIs and their correlation level.

Variable	Variable name	ERI correlation
p	Pressure (static pressure)	Poor
Dp/Dt	Material derivative of pressure	Some +
D^2p/Dt^2	Second material derivative of pressure	Some
$(Dp/Dt)^2$	Material derivative of pressure, squared	Good
Dp_d/Dt	Material derivative of dynamic pressure	Poor
R_c	MTR during condensation	Poor
$D\rho/Dt$	Material derivative of density	Poor
$D\alpha_l/Dt$	Material derivative of liquid volume fraction	Poor
<i>PPD1</i>	Potential power density 1	Some +
<i>PPD2</i>	Potential power density 2	Good
P_a	Acoustic power	Poor

Fig. 17 shows the two best ERIs, $(Dp/Dt)^2$ and $PPD2$, and how well the location of the maxima correlates with that of erosion on the hardware. These two indicators targeted the correct location and showed significantly higher peak values on the original design. They also reproduce the distinctive pattern of erosion seen on the original hardware design on the guide.

These two ERIs can be applied to product design and development. For example, an existing production component that is free of erosion can be used as a control case to establish the distribution and intensity of the ERIs. The ERIs for any new or modified design can then be compared with the control case. A significant worsening of the ERI characteristics would indicate a region at risk of erosion. In this way, considerable time and cost could be saved during product development.

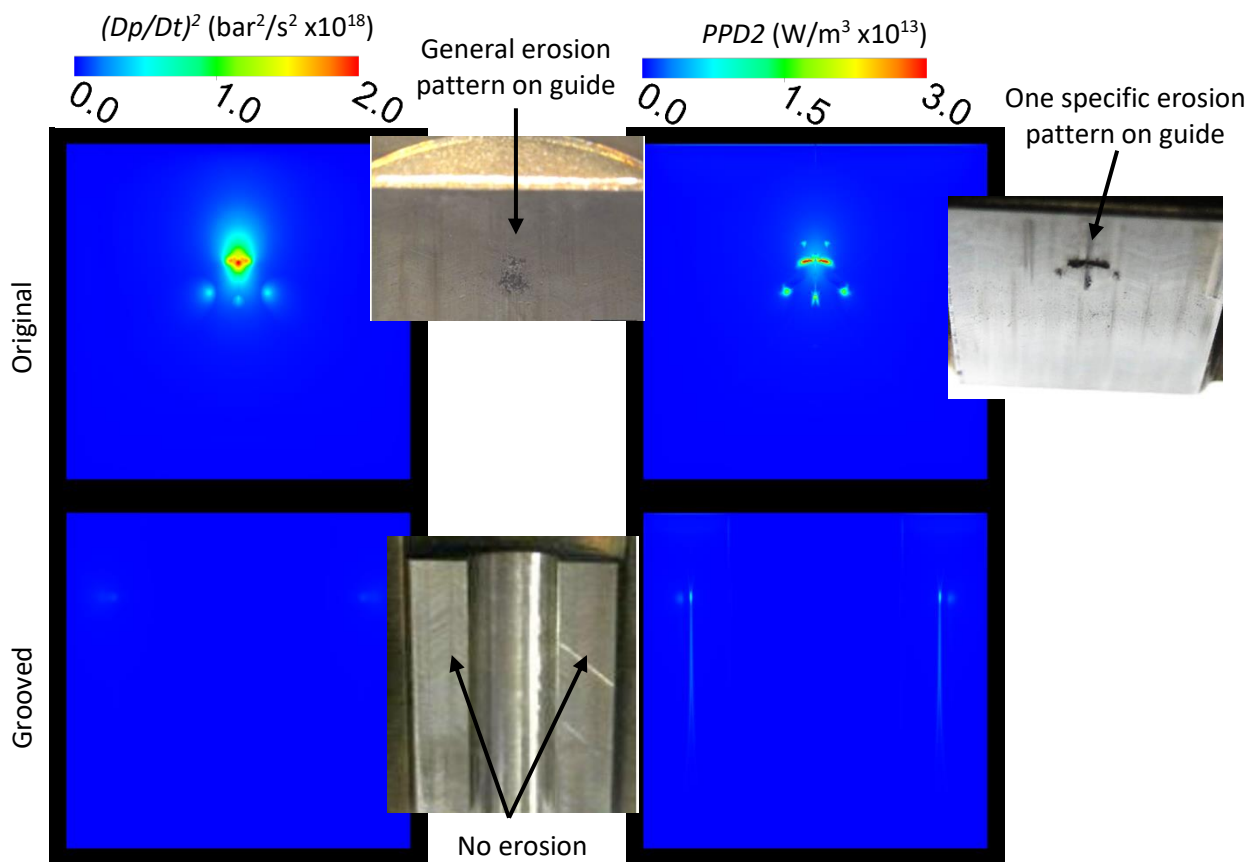


Fig. 17 – The two most successful ERIs and images of hardware

6 - Conclusion

The fluid dynamics within a shoe and guide assembly located below the pumping plunger in a high-pressure fuel pump were investigated. Two designs were considered, the original, which experienced non-critical cavitation erosion, and a modified design, that had a groove in the guide face which eliminated the erosion. The region of interest was the thin, liquid filled gap between the shoe and its guide. The dynamic CFD simulations provided understanding and visualization of the cavitation characteristics in the gap. These results confirmed that the creation and collapse of cavitation in this gap was caused by the expected small lateral movement of the shoe, which occurred near the top of the pumping stroke.

The results for the two different designs were further analysed to evaluate several potential ERIs. Each indicator was assessed by comparing the distribution of its maximum values with images of cavitation erosion on the hardware. Almost all of the ERIs targeted the correct region at risk of erosion on the original design. It is important to note however, that it was only by comparing with the results of the undamaged design that a reliable assessment could be made. Accordingly, the ERIs that gave the most accurate results were $(Dp/Dt)^2$ and $PPD2$ (Eq. 8). $(Dp/Dt)^2$ was newly derived for this research and $PPD2$ was proposed by Fortes-Patella et al [26]. It is now anticipated that using these two ERIs to guide product design and development will save considerable time and cost.

Acknowledgment

The authors would like to thank Delphi Technologies for providing experimental results and product details. Furthermore, we thank City, University of London, for providing computational resources.

References

- [1] T. M. Mitchell and F. G. Hammitt, "Collapse of a spherical bubble in a pressure gradient," in *ASME Cavitation Forum*, Detroit, 1970.
- [2] P. Koukouvini, M. Gavaises, A. Georgoulas and M. Marengo, "Compressible simulations of bubble dynamics with central upwind schemes," *Int. J. of CFD*, vol. 30, no. 2, 2016.
- [3] J. R. Blake, G. S. Keen, R. P. Tong and M. Wilson, "Acoustic cavitation: the fluid dynamics of non-spherical bubbles," *Philosophical Transactions of the Royal Society of London Series A-Mathematical Physical and Engineering Sciences*, vol. 357, no. 1751, pp. 251-267, 1999.
- [4] D. Dowson and C. M. Taylor, "Proceedings of the 1st Leeds-Lyon Symposium on tribology," in *Mechanical Engineering Publications*, 1974.
- [5] P. Dellis and C. Arcoumanis, "Cavitation development in the lubrication film of a reciprocating piston-ring assembly," *Journal of Engineering Tribology*, vol. 218, no. 157, 2004.
- [6] A. Unsworth, D. Dowson and V. Wright, "'Cracking joints'. A bioengineering study of cavitation in the metacarpophalangeal joint," *Annals of the rheumatic diseases*, vol. 30, no. 4, 1971.
- [7] J. B. Hunt, A. J. Ryde-Weller and F. A. H. Ashmead, "Cavitation between meshing gear teeth," *Wear*, vol. 71, no. 65, 1981.
- [8] J. A. Cole and C. J. Hughes, "Oil flow and film extent in complete journal bearings," *Proc. Instn. Mech. Engers.*, vol. 170, pp. 499-510, 1956.
- [9] Y. Zhou, J. He and F. G. Hammit, "Cavitation erosion of diesel engine wet cylinder liners," *Wear*, vol. 76, 1982.
- [10] S. R. Gonzalez-Avila, E. Klaseboer, B. C. Khoo and C. Ohl, "Cavitation bubble dynamics in a liquid gap of variable height," *Journal of Fluid Mechanics*, vol. 682, pp. 241-260, 2011.
- [11] P. A. Quinto-Su, K. Y. Lim and C. Ohl, "Cavitation bubble dynamics in microfluidic gaps of variable height," *Physical Review E*, vol. 80, 2009.
- [12] C. T. Hsiao, J. K. Choi, G. L. Chahine, T. A. Hay, Y. A. Ilinskii, E. A. Zabolotskaya, M. F. Hamilton, G. Sankin, F. Yuan and P. Zhong, "Modelling single- and tandem-bubble dynamics between two parallel plates for biomedical applications," *Journal of Fluid Mechanics*, vol. 716, pp. 137-170, 2013.
- [13] J.-P. Franc and J.-M. Michel, *Fundamentals of Cavitation*, New York: Kluwer Academic Publishers, 2005.
- [14] D. Parkins and W. Stanley, "Characteristics of an oil squeeze film," *Journal of Lubrication Technology*, vol. 104, no. 4, pp. 497-502, 1982.
- [15] Rayleigh, "On the pressure development in a liquid during the collapse of a spherical cavity," *Philosophical Magazine*, vol. 34, no. 200, pp. 94-98, 1917.
- [16] T. Okada, Y. Iwai and K. Awazu, "A study of cavitation bubble collapse pressures and erosion part 1: A method for measuring of collapse pressures," *Wear*, vol. 133, pp. 219-232, 1989.
- [17] A. Philipp and W. Lauterborn, "Cavitation erosion by single laser-produced bubbles," *J. Flui Mech.*, vol. 361, pp. 75-116, 1998.

- [18] S. Joshi, J. Franc, G. Ghiglitti and M. Fivel, "SPH modelling of a cavitation bubble collapse near an elasto-visco plastic material," *Journal of the Mechanics and Physics of Solids*, vol. 125, pp. 420-439, 2019.
- [19] S. Roy, J. Franc, C. Pellone and M. Fivel, "Determination of cavitation load spectra - part 1: static finite element approach," *Wear*, vol. 344, pp. 110-119, 2015.
- [20] M. Gavaises, D. Papoulias, A. Andritotis and E. Giannadakis, "Link between cavitation development and erosion damage in diesel injector nozzles," *SAE Technical Paper 2007-01-0246*, 2007.
- [21] N. Soda and Y. Tanaka, "Cavitation erosion of a flat surface near a rotating shaft," *Wear*, vol. 74, pp. 275-286, 1982.
- [22] P. Koukouvinis, G. Bergeles and M. Gavaises, "A new methodology for estimating cavitation erosion: application on a high speed cavitation test," in *11th World Congress on Computational Mechanics*, Barcelona, Spain, 2014.
- [23] P. Koukouvinis, G. Bergeles and M. Gavaises, "A cavitation aggressiveness index within the Reynolds averaged Navier Stokes methodology for cavitating flows," *Journal of Hydrodynamics*, vol. 27, no. 4, 2015.
- [24] P. Koukouvinis, N. Mitroglou, M. Gavaises, M. Lorenzi and M. Santini, "Quantitative predictions of cavitation presence and erosion-prone locations in a high pressure cavitation test rig," *Journal of Fluid Mechanics*, vol. 819, pp. 21-57, 2017.
- [25] P. Koukouvinis, M. Gavaises, J. Li and L. Wang, "Large eddy simulation of diesel injector including cavitation effects and correlation to erosion damage," *Fuel*, vol. 175, pp. 26-39, 2016.
- [26] R. Fortes-Patella, J. L. Reboud and L. Briancon-Marjollet, "A phenomenological and numerical model for scaling the flow aggressiveness in cavitation erosion," in *Cavitation Erosion Workshop*, Val de Reuil, 2004.
- [27] M. S. Mihatsch, S. J. Schmidt and N. A. Adams, "Cavitation erosion prediction based on analysis of flow dynamics and impact load spectra," *Physics of Fluids*, vol. 27, no. 10, 2015.
- [28] M. Lyon, J. McHattie and C. Cardon, "Delphi new diesel common rail family: focus on high pressure pumps," in *Fuel Systems*, London, 2015.
- [29] M. Winterbourn, M. Balin, R. Jorach, C. Soteriou, W. Tang and S. Zülch, "The Virtual Pump – Integrated Simulation of the High Pressure Diesel Common Rail Pump," in *Otto-von-Guericke-Universität*, Berlin, 2006.
- [30] J. Lang, G. Knoll, I. Thornthwaite, C. Soteriou, C. Lensch-Franzen and M. Kronstedt, "Simulation methods for elasto-hydrodynamically coupled hydraulic components," in *9th International Fluid Power Conference*, Aachen, 2014.
- [31] Ansys, Inc., "Ansys Fluent Theory Guide," SAS IP, Canonsburg, PA., 2013.
- [32] P. J. Zwart, A. G. Gerber and T. Belamri, "A Two-Phase Flow Model for Predicting Cavitation Dynamics," in *5th international Conference on Multiphase Flow*, Yokohama, Japan, 2004.
- [33] M. Brunhart, C. Soteriou, C. Daveau, M. Gavaises, P. Koukouvinis and M. Winterbourn, "Investigation on the removal of the cavitation erosion risk in a control orifice inside a prototype diesel injector Outlet Orifice Inlet," in *IMEchE Fuel Systems*, London, 2018.
- [34] C. Soteriou, R. Andrews and M. Smith, "Further studies of cavitation and atomization in diesel injection," *SAE Technical Paper 1999-01-1486*, 1999.
- [35] E. H. Ndiaye, J. Bazile, D. Nasri, C. Boned and J. L. Daridon, "High pressure thermophysical characterization of fuel used for testing and calibrating diesel injection systems," *Fuel*, vol. 98, 2012.
- [36] M. Chorażewski, F. Dergal, T. Sawaya, I. Mokbel, J. Grolier and J. Jose, "Thermophysical properties of Normafluid (ISO 4113) over wide pressure and temperature ranges," *Fuel*, vol. 105, pp. 440-450, 2013.
- [37] D. Bush, C. Soteriou, M. Winterbourn and C. Daveau, "Investigating hydraulic control components in high performance injectors," in *IMEchE Fuel Injection*, London, 2015.
- [38] F. G. Hammit, "Observations on cavitation damage in a flowing system," *ASME Journal of Basic Engineering*, pp. 347-367, 1963.